Influence of Vacuum Support on the Fatigue Life of AlSi9Cu3(Fe) Aluminum Alloy Die Castings

Péter Szalva and *Imre Norbert Orbulov*

High-pressure die casting (HPDC) is a near-net-shape process that produces high quality castings with narrow dimensional tolerances. The HPDC castings are being increasingly used due to good flexibility and high productivity, especially for the automotive industry. Depending on the location of the cast components, there are ever more complex geometries and increasing strength requirements that can be achieved by the application of vacuum-assisted die casting (VPDC). The most specific features of the HPDC process are the rapid mold filling, high cooling rate and intensification pressure. As a consequence of these highlighted features, the process generally leads to the formation of casting defects, such as gas porosity, shrinkage, and entrapped oxide films. However, the VPDC casting process is capable to significantly reduce the amount of these casting defects. The aim of this work is to compare the HPDC and VPDC castings' high-cycle fatigue behavior and to describe how the casting defects affect the fatigue failure. Before the fatigue tests, the samples were investigated with non-destructive (NDT) materials testing methods such as hydrostatic weighing, x-ray, and computer tomography (CT) to characterize the gas pore and shrinkage pore populations of the material. The AlSi9Cu3(Fe) aluminum alloy castings have been subjected to constant amplitude load by uniaxial fatigue tests in the high-cycle fatigue region with a stress asymmetry ratios of $R = -1$ and $R = 0.1$. The resulting fracture surfaces are analyzed through light optical microscopy (LOM) and scanning electron microscopy (SEM). VPDC increased the number of cycles to fracture and decreased the scatter at the given load levels compared to conventional HPDC casting. Moreover, VPDC significantly decreased the porosity size and volume, and the occurrence of oxide flakes is also decreased, resulting in the improvement in the number of cycle to failure.

1. Introduction

High-pressure die casting (HPDC) is a near-net-shape manufacturing process that produces high-quality castings with narrow dimensional tolerances. The HPDC of aluminum castings are being increasingly used due to good flexibility and high productivity, especially for the automotive industry (Ref 1). Depending on the location of the cast components, there are ever more complex geometries and increasing strength requirements. Various techniques have been applied to meet these requirements. The application of vacuum in HPDC process is the vacuum-assisted die casting (VPDC). VPDC is promising a significant reduction in gas entrapment during die filling and through that oxide film reduction on the free liquid surface (Ref 2). The most specific features of the die casting

process are the rapid mold filling, high cooling rate and third phase of the casting known as intensification pressure. As a result of these highlighted features the process generally leads to the formation of variety of casting defects, such as porosities, shrinkages, and entrapped oxide films (Ref 3). These defects may significantly affect the load-bearing capability and fatigue properties of the castings.

Previous studies have reported that the mechanical properties of die cast AlSi9Cu3(Fe) casting specimens increases by decreasing the porosity level (Ref 4, 5). The fatigue strength of specimens, which are containing defect(s) is lower than that of the defect-free samples' (Ref 6). A few studies have been examined the effect of the casting defects on the fatigue properties, and they concluded that a combination of pores and oxide flakes cause a fatigue strength decrement. The reliable design of a die casting component requires the evaluation of high-cycle fatigue strength and fatigue life as well (Ref 7, 8).

The aims of this work are (i) to compare the HPDC and VPDC cast smooth specimens high-cycle fatigue (HCF) behavior and (ii) to describe what kind of casting defects affect the fatigue failure and lifetime. The AlSi9Cu3(Fe) secondary aluminum alloy was used in this study. The casting specimens were examined and classified in x-ray, hydrostatic weighing and computer tomography (CT). CT scan analysis was presented with the aim of characterizing the microshrinkage pore population of the material. The uniaxial fatigue tests were performed at two different load levels at the stress asymmetry factor (R) equal to −1 and 0.1, respectively. The uniaxial fatigue tests were run in load control mode and four load levels were defined at each stress asymmetry factor. The traditional fatigue design approach with Wöhler diagrams (S–N

Péter Szalva, Department of Materials Science and Engineering, Budapest University of Technology and Economics, Müegyetem rakpart 3, Budapest 1111, Hungary; and **Imre Norbert Orbulov**, Department of Materials Science and Engineering, Budapest University of Technology and Economics, Müegyetem rakpart 3, Budapest 1111, Hungary; and MTA-BME Lendület Composite Metal Foams Research Group, Müegyetem rakpart 3, Budapest 1111, Hungary. Contact e-mail: szalva@eik.bme.hu.

curves) does not take into account the influence of casting defects on fatigue life (Ref 9), which—however—has a strong influence on the samples. The cycle to failure for same load levels were evaluated by the two-parameter Weibull analysis. On the fatigue lifetime region the 'Basquin law' was fitted with the least square method for the same confidence level at the given load levels by the application of the Weibull distribution-based analysis. The resulting fracture surfaces were analyzed through light optical microscopy (LOM) and scanning electron microscopy (SEM) in order to reveal the type of defects at the origin of the failure.

Casting specimens were produced by horizontal cold chamber HPDC machine. The application of vacuum in HPDC process was performed via vacuum system to obtain the significant reduction in the gas entrapment during die filling. Furthermore, to exhaust almost all of the air, steam and burnt gases, the HPDC and VPDC processes parameters were fixed, and the material chemical composition was monitored. Only the absolute pressure in the cavity was changed between the HPDC and VPDC casting trial.

2. Materials and Methods

2.1 Aluminum Casting Alloy

Fatigue specimens were made from secondary AlSi9-Cu3(Fe) (EN AC 46000) aluminum alloy. The secondary alloys are cheaper, which provides a wide range of uses. The melted castings actual chemical composition was measured four times during the casting trial and the averaged value is tabulated in Table 1. In generally, the die casting alloys are usually secondary alloys, where the iron content is in the range of 0.6-1.1 wt.% in order to avoid the molten metal soldering to die mold. On the other hand, this amount of iron cause intermetallic compounds, which decrease the ductility of the castings. Therefore, grain refining alloys, namely Sr, Mn, Be, and Ca are used to improve the strength and neutralize the effect of the brittle compounds by substituting them with less harmful morphology. In this case the iron content is suitable between 0.6-1.0 wt.% according to the materials standard (Ref 10). This casting alloy has favorable mechanical properties due to its relatively high copper content, which makes the precipitation hardenability available for the casting.

The aluminum alloy was melted in a gas heated furnace with less than 25% regenerated scrap. The aluminum melt was treated with rotary degassing and additional cleaning flux Thermal M35 and degassing with nitrogen gas 12 l/min during 6 min. The casting trial was performed with one heat and dosed with automatic ladling from a holding furnace, at the liquid metal temperature of 700 °C.
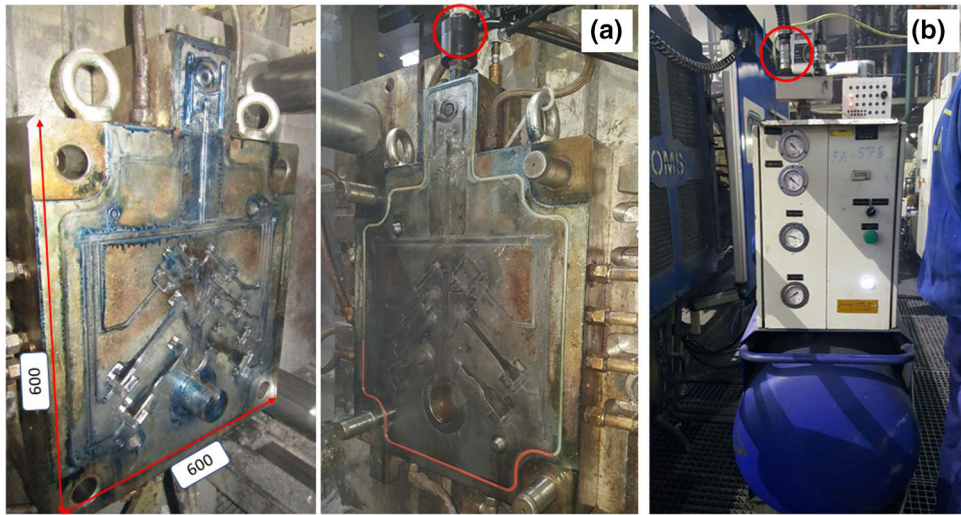
2.2 HPDC and VPDC Parameters

The specimens were produced by an OMS 450 cold chamber die casting machine with a locking force of 4.7 MN. The tool temperature was balanced with Tool-Temp TT-390/2 with oil circuit channels in the die at 170 °C. The plunger tip diameter was 60 mm, the plunger velocity was 0.19 ms^{-1} in the first phase and 2.9 ms^{-1} in the second phase, and the intensification pressure was 720 bars in the third phase. The filling degree was 0.39 of the shot chamber. The conventional casting was performed firstly, where the adjusted pressure level was atmospheric. The in-gate cross section was 136 mm^2, and the venting cross section was 33 mm^2. The summarized air volume in the mold was 289.3 cm^3, and 517 cm^3 in the chamber. The casting parameters were determined by filling simulation. The test results in real conditions are able to use as validation of virtual results in a further investigation. The vacuum-assisted casting was performed secondly, when the vacuum was applied by valve. The vacuum-assisted casting is capable to significantly reduce the amount of casting defects (Ref 11). The connected vacuum system is consisting of a tank equipped with vacuum pump and valve in order to exhaust the air, gases and humidity (Ref 12). The vacuum valve was a VDS kinetic valve connected directly to the die tool (Fig. 1) and connected to the tank by a flexible pipe. The tool was gasketed by silicone sealing. The vacuum was measured by Thyracont digital vacuum meter type VD81, and the connection plug is marked by red circle in Fig. 1a. The vacuum unit in Fig. 1b. provides the 120 ± 10 mbar absolute die cavity air pressure during the casting trial. The castings were tested in 'T1' controlled cooling from casting and natural aged condition.
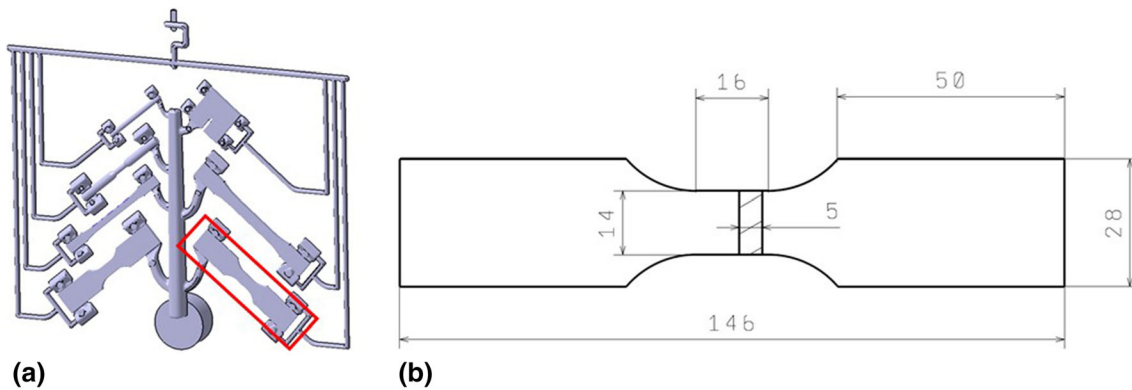
2.3 Die Casting Specimen

The casting specimens bunch is depicted in Fig. 2, and this multi-specimen casting is composed for different mechanical tests. The flat unnotched fatigue test specimens with a nominal thickness of 5 mm were used for the uniaxial fatigue tests. The gauge length is 16 mm, and the width is 14 mm, respectively. The investigated fatigue specimen was trimmed from the casting bunch. The only modification on the cast-to-shape condition was the slight grinding of the flash by 800 mesh abrasive paper, without further machining. The roughness of the specimens has been measured over the gauge section surface having an average roughness value $R_a = 0.75 \pm 0.3$ μm and $R_z = 5.6 \pm 2$ μm.

The averaged static mechanical properties of the conventional and vacuum-assisted casting fatigue specimens are listed in Table 2, where the terms of the abbreviation are the ultimate tensile strength (UTS), the yield strength ($R_{p0.2}$), and the elongation to fracture (A). The results were evaluated according to ISO 6892-1:2016 (Ref 13) testing method 'B'. The tensile strength was measured on an Instron 5985 testing machine, with tensile rate of 1 mm min^{-1}, at room temperature, with gauge length of 10 mm.

Table 1 Chemical composition of AlSi9Cu3(Fe)

Alloy AlSi9Cu3(Fe)	Si, wt.%	Fe, wt.%	Cu, wt.%	Mn, wt.%	Mg, wt.%	Zn, wt.%	Ti, wt.%	Al
Elements	9.17	0.90	2.85	0.27	0.27	0.60	0.08	bal.

Fig. 1 Die tool: (a) both tool half and the vacuum valve connection; (b) vacuum unit.

Fig. 2 Casting bunch: (a) the investigated specimen marked by red rectangle; (b) the dimensions of the flat fatigue specimen.

Table 2 Averaged static tensile mechanical properties of HPDC and VPDC castings

	UTS, MPa	$R_{p0.2}$, MPa	A, %
HPDC	314 ± 5.6	183 ± 7.7	2.11 ± 0.16
VPDC	326 ± 3.5	187 ± 4.2	2.81 ± 0.08

2.4 Non-destructive and Destructive Testing and Fracture Surface Analysis

The two times 60 pieces conventional and vacuum-assisted casting fatigue specimens were randomly chosen from the casting trials. These sets were divided into two groups for both stress asymmetry factors. HPDC specimens were marked by 'Atm' the VPDC specimens were marked by 'Vac' and numbered from 1 to 60, if the specimen was scanned with CT there was marked by an additional 'P'. Preliminary investigations were performed on these four sets of casting specimen by non-destructive testing (NDT) as hydrostatic weighing (Ref 14) and x-ray inspections according to ASTM E505 (Ref 15). Hydrostatic weighing was carried out on all chosen specimens. The fatigue specimens were weighted in air and in water as well (Ref 16, 17), and their densities were determined according to the standard procedure (Ref 18). The given density of specimen takes the porosity into account. The porosity of the examined specimen can be calculated in the possession of the measured density and the theoretical density of the cast metal. The weighing scale was an Entris 6202-1S with ±0.01 g accuracy produced by Sartorius Lab. The x-ray analysis is capable to detect the size and the position (Ref 19) of the discontinuities. However, there is a limitation to detect the exact morphology and the detectable minimum defect size was 0.2 mm according to used Yxlon MU2000 x-ray machine. The 2D radiographs were recorded to investigate a large volume of the specimen and the probability of encountering large pores in the specimen.

According to the results of the volumetric porosity evaluation each set had 10 best pieces selected for computer tomography (CT), where 'best' means the lowest amount of porosity. The gauge lengths were inspected with CT to specify the porosity variability on each set of 10 pieces test specimen. The CT scan was a Phoenix v|tome|x c with an accelerating voltage of 240 kV and current of 160 μA, equipped with a cone-beam x-ray tube. The resolution of the CT which means

here the volume of the smallest element (voxel) in the reconstructed 3D images was 25 μm. The CT analysis was reconstructed by using GE's algorithm and the porosity analysis was done Volume Graphic Studio Max 3.2 software (Ref 20) and analyzed automatically. The detected discontinuities of the samples were analyzed to obtain quantitative information on pore sizes, morphologies and their location. The CT results showed excessive scattering of the pore volume and pore dispersion in the case of HPDC castings compared to VPDC castings. CT scan analysis was presented with the aim of characterizing the micro-shrinkage pore population of the material (Ref 21). The specimens from these four sets were assigned randomly to the different load levels, 2-2 test pieces were used at the two higher load levels, and 3-3 test pieces were used at the two lower load levels. The preliminary tests results were re-assigned to the pieces after the fracture in order to confirm, which defect initiated a crack.

Microstructural investigations were performed on a few HPDC and VPDC specimens to prove the reasons of the changes of the mechanical properties of static and dynamic cases. The microstructural observations were carried out by light optical microscopy (LOM) by Olympus BX51M. The resulting fracture surfaces were analyzed through LOM by Olympus SZX16 and scanning electron microscopy (SEM) analysis in order to reveal the type of defects at the origin of the failure. The SEM (Ref 22) equipped with an energy-dispersive x-ray analyser (EDX) by Zeiss Evo MA15 SEM machine (EHT = 20.00 kV). The fracture surfaces were studied to evaluate the crack initiation and propagation site by both kinds of microscopy. The aluminum oxide flake could not be detected by the applied non-destructive testing (Ref 23, 24), that is why the size and location of the oxides could only be investigated on the fracture surfaces.

2.5 Fatigue Tests

The castings were tested in 'T1' condition it means controlled cooling in water after casting and natural aging. The casting specimen were stored at room temperature for 2 months after casting, which provided a substantially stable condition in case of AlSi9Cu3(Fe) alloy (Ref 10). The uniaxial tension fatigue tests were performed on Instron 8800 servo-hydraulic testing machine, provided a maximum load range of ±25 kN. Tests were stopped when a drop in displacement of 0.2 mm was detected or if there was no crack in this case the fatigue strength for the specimens corresponds to 2×10^6 cycles of fatigue loading (Ref 25). The uniaxial fatigue tests were run in load control and sinusoidal loads with test frequency of 20 Hz at four different stress amplitudes as tabulated in Table 3, at the stress asymmetry ratios of $R = -1$ and $R = 0.1$, respectively. This is commonly used frequency for fatigue test for structural parts at the foundry, where the

castings produced. Not too low, therefore the tests can be performed in reasonable time and too high, avoiding significant heating in the samples. The reason for the two stress asymmetry ratios is that, these are often used in automotive component testing (Ref 26), and planned further investigation.

The cycles to failure for same load levels were evaluated by the two-parameter Weibull analysis approach (Ref 27). The Weibull analysis is capable to investigate the fatigue strength variability of the materials, which is arising from their defects.

The two-parameter Weibull distribution is described according to (Eq 1):

$$F_{(x;\alpha,\beta)} = 1 - \exp\left[-\left(\frac{x}{\alpha}\right)^{\beta}\right] \qquad (Eq\ 1)$$

where $F(x; \alpha, \beta)$ represent the probability that the fatigue strength is equal to or less than x. Using the equation of probability of survival $P(x; \alpha, \beta)$ the equation is (Eq 2):

$$P_{(x;\alpha,\beta)} = \exp\left[-\left(\frac{x}{\alpha}\right)^{\beta}\right] \qquad (Eq\ 2)$$

Equation 1 is converted to a straight line by taking double logarithms. In this way, by using the linear regression method for estimating the scale and shape parameters. The Weibull modulus β can be obtained from its slope (Eq 3):

$$\ln\{\ln[1/(1 - F(x; \alpha, \beta))]\} = \beta \ln x - \beta \ln \alpha \qquad (Eq\ 3)$$

The fatigue strength values were determined from experimentals, these values were arranged in ascending order ($x_1 \leq x_2 \leq x_3 \leq x_n$). The estimation for $F(x; \alpha, \beta)$ in (Eq 4) is widely used for the i 'th' fracture, from a total N result.

$$F(x; \alpha, \beta) = (i - 0.3)/(N + 0.4) \qquad (Eq\ 4)$$

The fatigue limit could be estimated by the Basquin law (Eq 5). The curve was fitted with the least square method for the same confidence level of each load level.

$$\sigma_D = CN^m \qquad (Eq\ 5)$$

The casting specimens were fixed in clamps (Fig. 3), both sides of the fixture surfaces were knurled, and the two times six M8 (10.9) screws were tightened uniformly by 20 Nm.

3. Results and Discussion

3.1 Microstructure and Porosity

The AlSi9Cu3(Fe) aluminum alloy castings were produced by conventional die casting under atmospheric pressure and vacuum-assisted die casting under 120 mbar absolute die cavity air pressure. The averaged volumetric porosity level on the

Table 3 Stress amlitudes at two different load levels

R	σ_{amp}, MPa	σ_{max}, MPa	σ_{min}, MPa	σ_{mean}, MPa	R	σ_{amp}, MPa	σ_{max}, MPa	σ_{min}, MPa	σ_{mean}, MPa
−1	125	125	−125	0	0.1	72	160	16	88
−1	135	135	−135	0	0.1	82	182	18.2	100
−1	150	150	−150	0	0.1	90	200	20	110
−1	180	180	−180	0	0.1	105	233	23.3	128

randomly selected two times 60 pcs specimens was 0.61% with 0.05 scatter in case of HPDC and 0.54% with 0.06 scatter in case of VPDC.

The microstructural analysis was performed to prove the mechanical properties improvement before the fatigue tests. The castings were produced with the same chemical composition. The typical microstructure of the HPDC castings near the surface is shown in Fig. 4a and at the center of the material in Fig. 4b, and typical sponge-shaped shrinkage defect in Fig. 4c.

Furthermore, the typical microstructure of the VPDC castings with the same magnification near the surface is shown in Fig. 5a, and at the center of the material in Fig. 5b, and typical porosity defect in Fig. 5c.

The typical microstructures did not show differences in the grain size of HPDC (Fig. 4) and VPDC (Fig. 5) specimen cross section at the same magnification and at the same location. The microstructures of cast aluminum alloy are quite sensitive to the solidification rate (Ref 28). The grains were observed in dendritic nature with random texture. The average grain size is almost same, and the phases are mainly α-Al (light grey) and Al-Si eutectic (grey). Although the AlSi9Cu3(Fe) die casting aluminum alloy has relatively high Fe content, typical sharp, needle-like Fe-rich compounds were not identified, thanks to the grain refiner. The most frequent intermetallic compounds is the polygonalgonal Al(Fe,Mn,Cr)Si phases (dark grey) as usual in case of die casting aluminum alloys, these particles also show a same morphology and dispersion. As it can be also seen in the figures, many pores were formed during conventional casting in spherical shape and complex morphology as a sponge-shaped shrinkage. Contrary, the size of the pores was significantly reduced, and the distribution was homogeneous in case of vacuum-assisted casting. Aluminum oxide flakes and cold joints were not observed in the inspected cross section.

3.2 Non-destructive Testing

The hydrostatic weighing and x-ray testings were performed on each specimen before fatigue test. The randomly chosen four times 10 pcs specimens were scanned by CT scan as well, and the post mortem identified critical defects were re-assigned.

The x-ray tested samples were classified as 'Level 1' according to ASTM E505 (Ref 15). Based on the standard test conditions were for aluminum alloys, each category of discontinuity, and the plate thicknesses 3.2 mm (1/8 inch) up to 9.5 mm (3/8 inch). However, it should be noted and emphasized, cold fills (B) and foreign materials (D) were not detected. The detection of oxide flakes and nonmetallic inclusions with the used NTD techniques were not possible, because of the nature and the thickness of these defects (Ref 29, 30). The detected inhomogeneities were material discontinuities, and these pores were identified as gas porosity (A) or shrinkage (C) or the combination of them. The limitation of the x-ray inspection to detect the exact morphology was the detectable minimum defect size of 0.2 mm. The 2D radiographs were recorded to investigate a large volume of material and the large pores in the specimen. However, failures due to gas porosity in all cases were large enough and x-ray detectable porosities.

Figure 6 shows a re-assign in the same section between a CT slice and the fracture surface for HPDC (Atm,P30) specimen. The CT shows the volume porosity determined by means of grey scale threshold for a flat fatigue specimen (Ref 21).
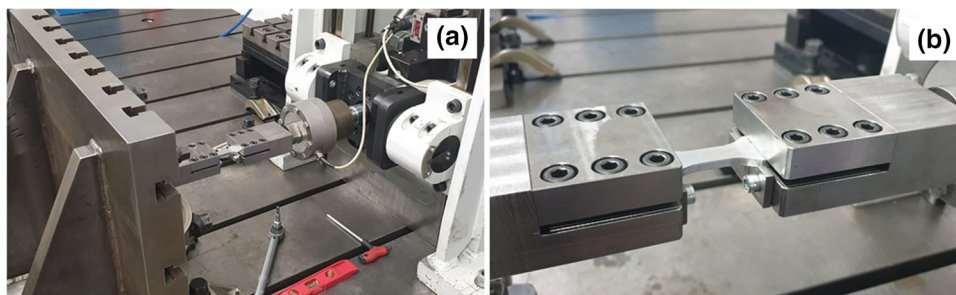

Fig. 3 Fatigue test equipment: (a) test environment; (b) fixture clamps with fatigue specimen.
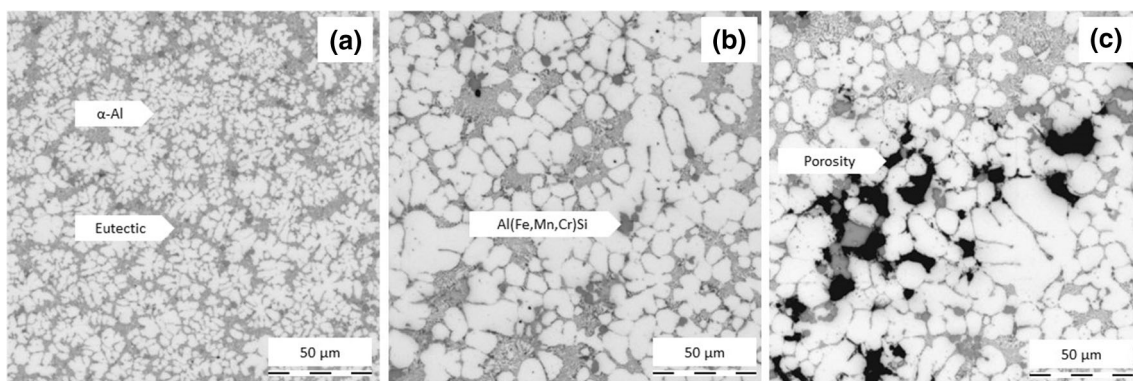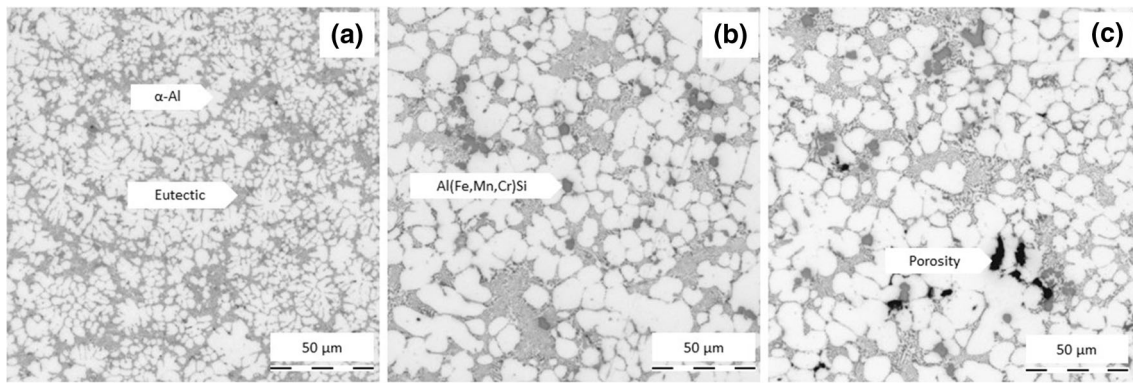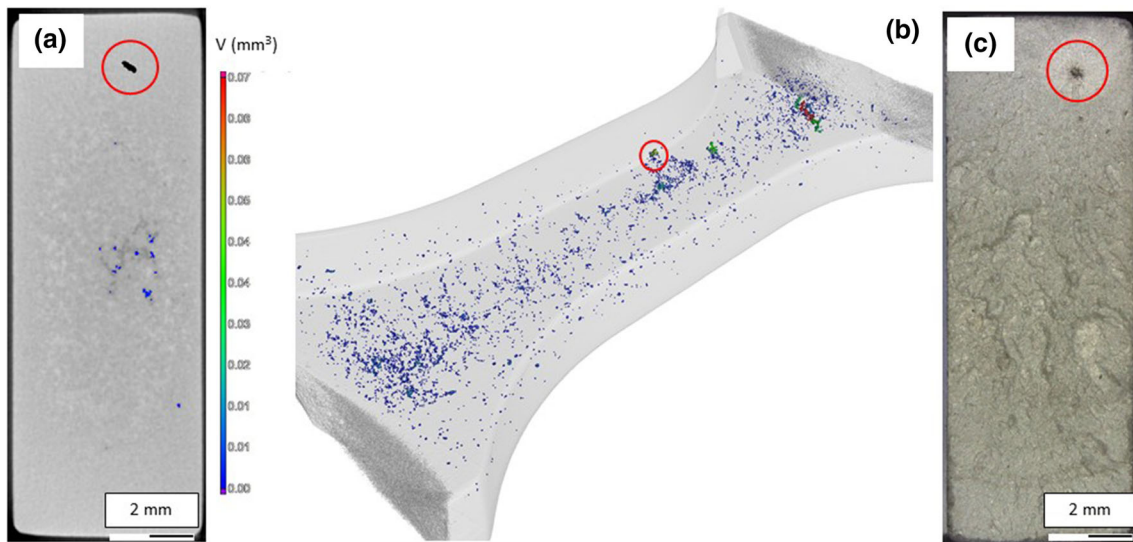

Fig. 4 Typical LOM micrograph of the HPDC specimen: (a) near the surface; (b) in the center; (c) casting defect.

Fig. 5 Typical LOM micrograph of the VPDC specimen: (a) near the surface; (b) in the center; (c) casting defect.


Fig. 6 Re-assign in the same section HPDC (Atm.P30): (a) CT slice of the specimen at the fracture; (b) isometric view of CT image of the specimen; (c) fracture surface by LOM.

Failure due to gas porosity was not identified in case of VPDC castings. If the main reason of the failure was a pore, there was a sponge-shaped shrinkage. The presence of the shrinkage surrounded by interdendritic porosity was the initiation site of the fracture.

Many HPDC and VPDC samples had a low porosity according to x-ray, which had been confirmed by CT scan analysis. CT scan analysis was presented with the aim of characterizing the micro-shrinkage pore population of the material as well. The critical defect size that does not lower the fatigue strength is close to the grain size of the material (Ref 31). Thus, the porosity lower than ~10 μm in diameter was removed to obtain a uniform distribution over the total porosity of the gauge length. The HPDC and VPDC castings typical gas porosity and shrinkage porosity are shown in the Fig. 7, where the typical defect sizes are also shown. The HPDC casting defects were randomly chosen from the set and present the general overview. The chosen VPDC defects were found just on a few samples. The CT results showed excessive scattering of the pore volume and pore dispersion in case of HPDC casting compared to the VPDC casting as shown in Fig. 7.

Regarding the porosities and shrinkages, the VPDC samples performed better quantitatively and qualitatively as well.
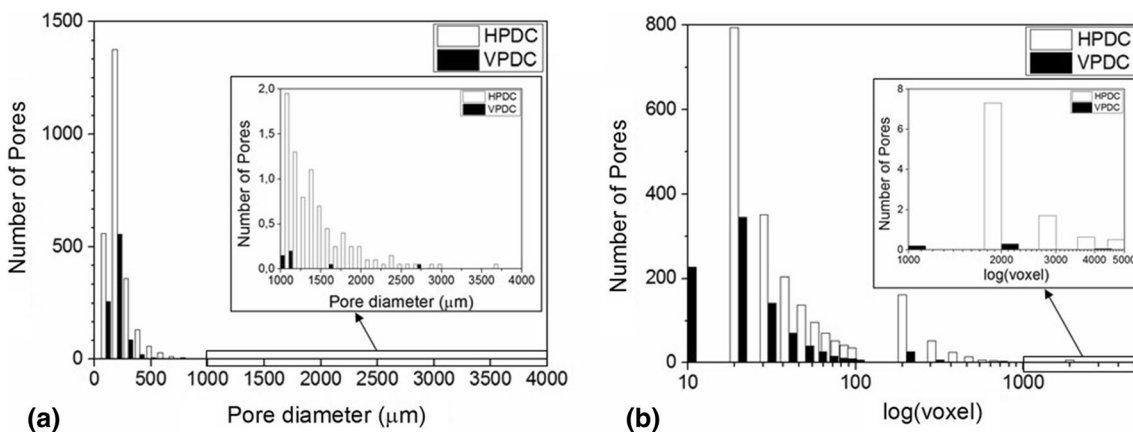
The identification of the defects is hard, and the results were discussed by a profession in x-ray investigations, as it is mentioned in the acknowledgements. The total porosity of the specimens and the total porosity of the gauge length are shown in Fig. 8. In order to compare the porosity of the HPDC and VPDC specimens. The volumetric porosity value shows only 0.07% differences, while CT scan results show a more significant difference of 0.25%. The major difference is that the clamping volume of the specimens showed large porosities by x-ray, which is included in the hydrostatic measurement of the total volume. The reason for the large porosity is explained by the die casting technology, the turbulence of the liquid during cavity filling, and cross section changes in the cavity. Based on the CT results, the volumetric porosity of the gauge length of the VPDC specimens is one-quarter compared to HPDC castings, and the standard deviation is only one-third compared to HPDC, respectively. On the other hand, the method to determine the porosities by weighing can be considered incorrect for these sample geometries at least. The hydrostatic weighing method is at best calming that the vacuum
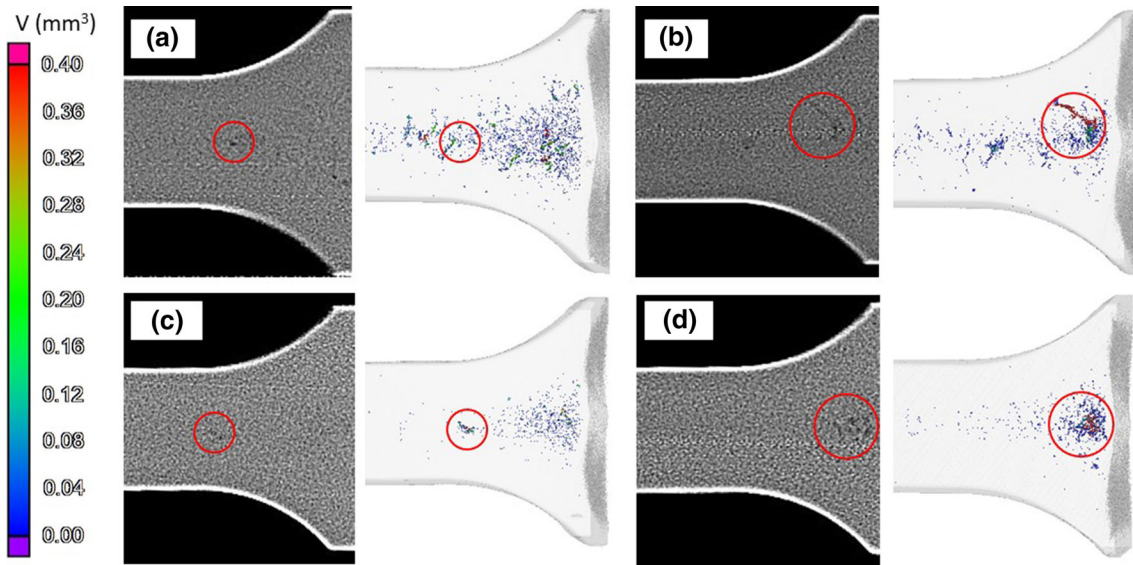
Fig. 7 Casting pore defects in the material: (a) gas porosity of HPDC (Atm.P11) 0.27%; (b) shrinkage porosity of HPDC (Atm.P18) 0.33%; (c) gas porosity of VPDC (Vac.P10) 0.059%; (d) shrinkage porosity of VPDC (Vac.P5) 0.109%.

works properly. Nevertheless, quantitative assessment will never be possible this way.

The averaged number of different size porosites expressed in microns, and in voxels, respectively, is shown in Fig. 9. The reason that the voxel plot is in logarithmic scale versus number of averaged porosity occurrences in the given range is the better representation of the scatter of the low volume porosity. The averaged number of pores of VPDC specimens is one-quarter compared to HPDC specimens. Furthermore, the occurrence of porosity diameter higher than 500 μm in case of VPDC is quite rare. The averaged number of pores of VPDC castings in the porosity voxel volume point of view are one-third compared to HPDC castings. The occurrence of the porosity volume higher than 400 voxel in case of VPDC castings is also quite rare.

3.3 Fatigue Tests

The uniaxial fatigue tests have been performed at two different stress asymmetry ratios: fully reversed $R = -1$ fatigue test firstly, and pulsating load $R = 0.1$ on the HPDC and VPDC test specimens. The uniaxial fatigue tests were run with load

Fig. 8 HPDC and VPDC castings porosity comparison.

Fig. 9 Averaged number of porosity in the given range: (a) the number of porosity vs. porosity diameter in μm; (b) the number of porosity vs. porosity in voxel in logarithmic scale.
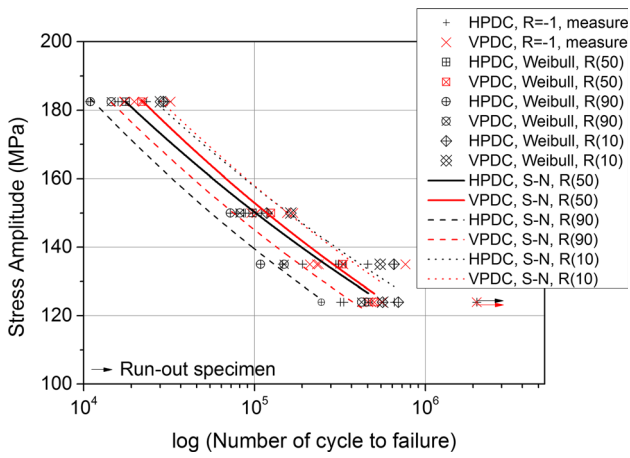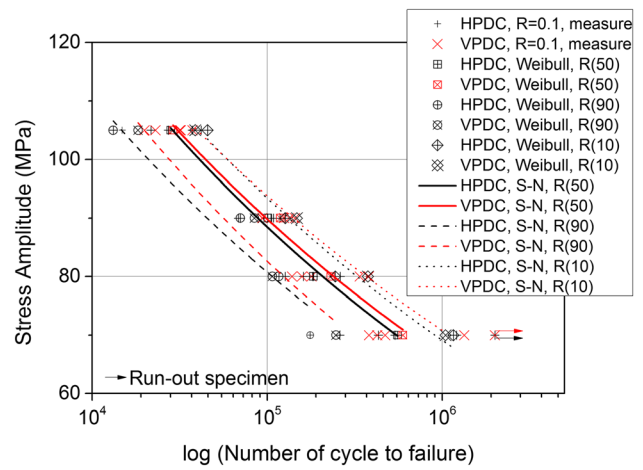
Fig. 10 The S–N curves of investigated casting specimens at stress asymmetry factor of $R = -1$ of HPDC and VPDC castings, at the reliability of 50% (S–N curve), 10 and 90%, respectively.

control, and four single load levels were performed at each stress asymmetry ratio. All specimens have been tested at room temperature with constant frequency of 20 Hz with sinusoidal waveform. The traditional fatigue design approach with Wöhler diagrams (S–N curves) does not take into account the influence of casting defects on fatigue life (Ref 9). The cycle to failure for the different stress asymmetry ratios were evaluated by the two-parameter Weibull analysis. The fatigue life region was fitted with the least square method for the same confidence level of load and for this the 'Basquin law' (Eq 5) was used. The S–N curves for $R = -1$ stress asymmetry ratio are shown in Fig. 10, and S–N curves for $R = 0.1$ stress asymmetry ratio are shown in Fig. 11, the number of cycle to failure plotted at the specified stress levels. The fatigue strength for the specimens corresponds to 2×10^6 cycles of fatigue loading in the current study. The fatigue strength for higher cycle to failure will be investigated in a later study. The castings, which withstand the 2×10^6 cycle has been tested with a dye penetrant liquid surface examination, but macroscopic initiation sites were not identified. The brittle fracture cracks spread extremely rapidly, with very little accompanying plastic deformation.

The S–N curves of the VPDC specimens in case of $R = -1$ is shifted to the right compared to the S–N curve of the HPDC specimens. The slopes of the S–N curves are same in the case of VPDC specimens compared to the slopes of the HPDC specimen, and the curves data are detailed in the Table 4 based on Eq 5. The averaged number of cycles to failure at $R = -1$ shows approximately +20% increment in case of VPDC based on the HPDC results. The slopes of the S–N curves at $R = 0.1$ are slightly higher in the case of VPDC compared to the slopes of the HPDC specimen, and the data of the curves are also detailed in the Table 4. The averaged number of cycles to failure at $R = 0.1$ shows approximately +16% increment in case of VPDC specimens. In fact, given the slope of the Basquin curve approximately equal to $m = 0.11$ in case of $R = -1$ (Table 4), the +20% increase in fatigue life means a +2% increase in fatigue strength. Furthermore, given the slope of the Basquin curve approximately equal to $m = 0.13$ in case of $R = 0.1$ (Table 4), the +16% increase of fatigue life means a +4% increase in fatigue strength.

The scatter of the test series on HPDC specimens is higher than the scatter on the VPDC castings at both stress asymmetry

Fig. 11 The S–N curves of investigated casting specimens at stress asymmetry factor of $R = 0.1$ of HPDC and VPDC castings, at the reliability of 50% (S–N curve), 10% and 90%, respectively.

Table 4 S–N curves data for HPDC and VPDC specimens at $R = -1$ and $R = 0.1$ stress asymmetry ratio

Reliability (50%)	$R = -1$		$R = 0.1$	
	m …	C MPa	m …	C MPa
HPDC S–N curve	−0.112	544.8	−0.138	432.1
VPDC S–N curve	−0.118	593.2	−0.132	412.5

factors. Regarding the scatter on the number of cycles to failure, they are increasing when the stress level decreases in each case. This explains the scissor-like widening of the reliability of the S–N curves. Furthermore, at a given stress level, the scatter increases when the detected biggest pore diameter increases. The crack initiation was principally driven by casting defects in the case of HPDC castings. Contrary, the crack initiation was principally driven by a conventional fatigue in the case of VPDC castings. This discrepancy is explained by the presence of small, macroscopic flaws (pores) or cracks (oxide flakes) that always exist under normal conditions at the surface and within the interior of a cast body. These flaws decreased the fatigue strength, because an applied stress may be amplified or concentrated at the crack tip (stress concentration effect, stress raiseres), and the magnitude of this amplification is depending on the crack orientation and geometry (Ref 32). The effect of the stress raisers is even more significant in brittle materials. The quality of the cast parts strongly depends on the geometry (Ref 8). In this study, a generalized experimental plan was performed to study the basic phenomenon on model samples.

3.4 Analysis of the Fracture Surfaces

The fracture surfaces of the fatigue specimens were examined with LOM to reveal the type of the defect and with SEM to identify the crack initiation sites. The inspections were performed only after fracture. The fatigue cracks initiation sites

were classified into four different cases (Fig. 12). The classification of these four types of initiation regions are oxide film entrapment (Fig. 12a), pores as gas porosity (Fig. 12b), solidification shrinkage (Fig. 12c), and defect-free fatigue fracture (Fig. 12d) initiated by crystallographic features (conventional fatigue). Although this classification presents the typical casting defects and a typical defect-free fracture surfaces, the selection of structural image spots and defects were arbitrary. These defects cause a material discontinuity in the castings where the fatigue fracture could be more easily initiated.

The typical transition zone from the smooth and regular (fatigue) initiation area to the irregular (brittle) one was identified in the case of defect-free fatigue failure. The appearance of aluminum castings fatigue failures is often described as brittle because of the little gross plastic deformation and fairly smooth fracture surfaces (Ref 5). The selection of fracture surfaces to LOM images remains the same based on the SEM images. Three main zones can be distinguished (Fig. 13): (i) The initiation zone shows bright area corresponds to the stable fatigue crack propagation phase, the borderline is marked by dashed red line, macroscopically, these sites appear as 'beach' marks (Fig. 13d), which represent delays in the fatigue loading cycle; (ii) The transition zone is narrow and show rapid changes of surface roughness because of rapid crack propagation, this borderline is marked by doted red line; (iii) The final static fracture of the specimen was occurred suddenly just in a few cycles, and shows river pattern (Fig. 13a, c, d) represented by a V-shaped 'chevron' mark (Ref 32) (Fig. 13c–d).

If the initiation site was not defect-free, the fracture surface showed differences just in the initiation zone. At the location of larger pores or sponge-shaped shrinkages as they are greater stress concentrators, they initiated the cracks. The shrinkages with sharp corners are more dangerous stress concentrators. The aluminum oxide flakes or an 'older' and therefore thicker oxide film can also indicate crack initiation. The appearance of
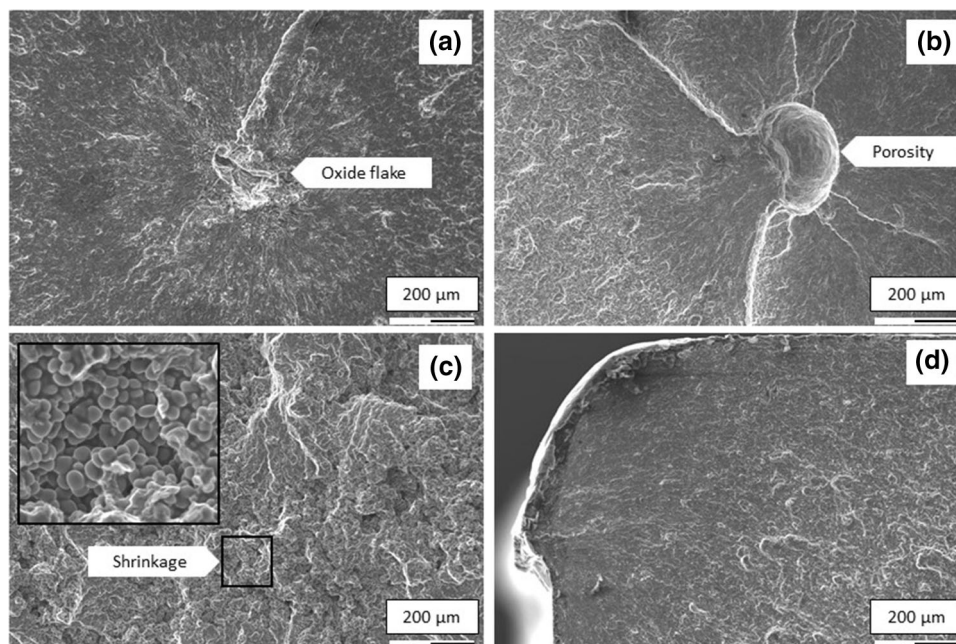
Fig. 12 SEM images of initiation regions: (a) oxide film entrapment HPDC (Atm.4); (b) gas porosity HPDC (Atm.42); (c) shrinkage HPDC (Atm.41); (d) casting defect-free fatigue fracture VPDC (Vac.28).
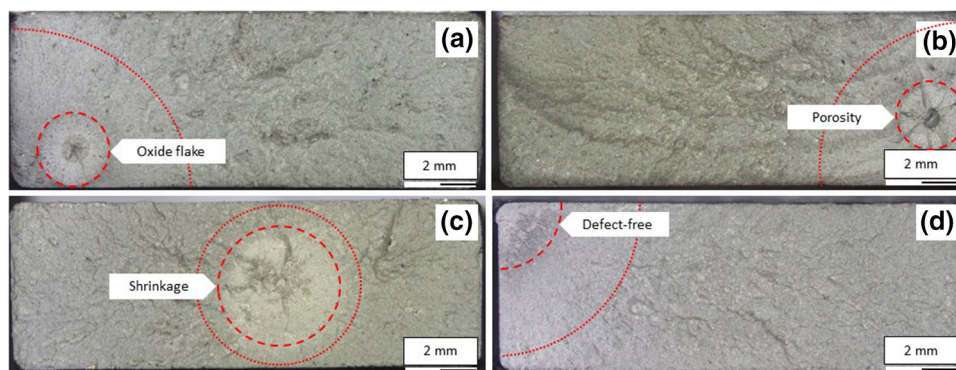
Fig. 13 Fracture surface of the casting specimen, red area indicates the SEM regions: (a) oxide film entrapment HPDC (Atm.4); (b) gas porosity HPDC (Atm.42); (c) shrinkage HPDC (Atm.41); (d) casting defect-free fatigue fracture VPDC (Vac.28).

the aluminum oxide flake is dark-gray oxidized skin, this defect formed during casting process (Fig. 13a). The oxide flake is folded in the liquid and solidified in a random orientation in the volume. That was observed during the LOM inspection, if the cracks were initiated by gas pores, and they were often surrounded by an oxide flake. To judge the initiation site of the fracture surface by naked eyes based on the previously performed LOM inspection, the bright spots were clearly gas pores, the dark-grey spots were mainly folded oxide inclusions. The vacuum-assisted castings are more resistant to break. The fracture profile in the most cases of VPDC specimens also show a defect-free fatigue failure resulting in longer lifetime, since there are no active initial stress-concentrators and the failure requires more energy investment.

The identified defects are typical casting defects, but their occurrence is different in the whole sample. In case of tested 20/22 pcs ($R = -1$ and $R = 0.1$) HPDC flat specimens 5/3 pcs of the specimens showed oxide inclusion, 5/8 pcs of the samples showed pores, and the remaining samples of the set showed classic defect-free fatigue fracture, which initiated from one localized point as crystallographic initiation. The cracks due to pore were mostly initiated by the shrinkage pores, and only 2/2 pcs of these samples were failed by gas porosity.

Furthermore, in case of tested 20/20 pcs ($R = -1$ and $R = 0.1$) VPDC flat specimens 0/2 pcs of the specimens showed oxide inclusion, 0/3 pcs of the casting failed by shrinkage pore, and sample failed by gas porosity was not detected, and the remaining samples of the set showed fatigue fracture with crystallographic initiation. However, these localized points were not limited to a single area as sharp corners, and the middle of the specimen wall could be also the starting point of the crack.

4. Conclusions

Uniaxial fatigue tests with two stress asymmetry factors of $R = -1$ and $R = 0.1$ have been performed on AlSi9Cu3(Fe) aluminum alloy casting specimens within a high-cycle fatigue (HCF) regime. The samples were produced by high-pressure die casting (HPDC) and vacuum-assisted high-pressure die casting (VPDC). The castings were preliminary tested by NDT techniques, and these results were re-assigned to the fracture surfaces after the fatigue test. Microstructural investigations were also performed in order to identify the microstructural constituents. The fatigue fracture surfaces were inspected by LOM and SEM to identify the initiation site of fracture and to determine the casting defect.

The slope of the S–N curves in case of HPDC specimens is $m = -0.112$ at $R = -1$ and $m = -0.138$ at $R = 0.1$. The slope of the S–N curves in case of VPDC specimens is $m = -0.118$ at $R = -1$ and $m = -0.132$ at $R = 0.1$. The significant, approximately +20% improvement in fatigue life at $R = -1$, and also significant approximately +16% improvement in the fatigue life at $R = 0.1$ the number of cycles to failure. In fact, given the slope of the Basquin curve approximately equal to $m = 0.11$ in case of $R = -1$ (Table 4), the +20% increase in fatigue life means a +2% increase in fatigue strength with the VPDC process as compared to the HPDC process. Furthermore, given the slope of the Basquin curve approximately equal to $m = 0.13$ in case of $R = 0.1$ (Table 4), the +16% increase in

fatigue life means a +4% increase in fatigue strength with the VPDC process as compared to the HPDC process. The reduction in scatter of number of cycles to failure was originated from the decrease in porosity volume fraction and decrease in porosity size in the specimens produced by vacuum-assisted die casting.

The detected third-quarter (75%) reduction in volumetric porosity by vacuum-assisted casting can improve the stress distribution in the castings, while the fatigue life increased. Fracture due to gas pores or oxide flake is not exactly separable, because the cracks were initiated by gas pores there were often surrounded by an oxide flake. Cracks were initiated in many cases by oxide flakes and pores in conventionally cast (HPDC) specimens, which are typical casting defects. It was found that the oxide flake detached from the matrix to form a crack before failure. Fatigue failure due to pore was quite rare, and fracture caused by oxide film was detected just in two cases in the given sample set produced by VPDC.

Failure due to sponge-shaped shrinkage on the investigated specimens could only be detected by CT. The large porosities that caused fatigue fracture were also detectable by x-ray. The problem is the repeatability of defects in the casting volume. Nevertheless, it was confirmed that VPDC gives more favorable mechanical characteristics. Higher number of fatigue tests will be performed to investigate the defects influence on the number of cycles to failure.

References

1. J. Linder, A. Arvidsson, and J. Kron, The Influence of Porosity on the Fatigue Strength of High-Pressure Die Cast Aluminium, *Mater. Struct.*, 2006, **29**(5), p 357–363. https://doi.org/10.1111/j.1460-2695.2006.00 997.x

2. X. Dong, X. Zhu, and S. Ji, Effect of Super Vacuum Assisted High Pressure Die Casting on the Repeatability of Mechanical Properties of Al-Si-Mg-Mn Die-Cast Alloys, *J. Mater. Process. Technol.*, 2019, **266**, p 105–113. https://doi.org/10.1016/j.jmatprotec.2018.10.030

3. X. Cao and J. Campbell, Oxide inclusion defects in Al-Si-Mg cast alloys, *Can. Metall. Q.*, 2005, **44**(4), p 435–448. https://doi.org/10. 1179/cmq.2005.44.4.435

4. P. Szalva and N.I. Orbulov, The Effect of Vacuum on the Mechanical Properties of Die Cast Aluminum AlSi9Cu3(Fe) Alloy, *Int. J. Metalcast.*, 2019, **2019**, p 1–12. https://doi.org/10.1007/s40962-018-00302-z

5. A.K.M. AzizAhamed and H. Kato, Influence of Casting Defect on Tensile Properties of ADC12 Aluminum Alloy Die-Castings, *Mater. Trans.*, 2008, **49**(7), p 1621–1628. https://doi.org/10.2320/matertrans. F-MRA2008814

6. L. Lattanzi, A. Fabrizi, A. Fortini, M. Merlin, and G. Timelli, Effect of Microstructure and Casting Defects on the Fatigue Behavior of the High-Pressure Die-Cast AlSi9Cu3(Fe) Alloy, *Procedia Struct. Integr.*, 2017, **2017**, p 505–512. https://doi.org/10.1016/j.prostr.2017.11.119

7. A. Rotella, Y. Nadot, M. Piellard, R. Augustin, and M. Fleuriot, Fatigue Limit of a Cast Al-Si-Mg Alloy (A357-T6) with Natural Casting Shrinkages Using ASTM Standard X-Ray Inspection, *Int. J. Fatigue*, 2018, **114**, p 177–188. https://doi.org/10.1016/j.ijfatigue.201 8.05.026

8. A. Rotella, Y. Nadot, S. Richard, S. L'Heritier, and A. Roy, Fatigue Life of Cast Al Component, *Procedia Eng.*, 2015, **133**, p 211–222. https://doi.org/10.1016/j.proeng.2015.12.661

9. J. Linder, A. Arvidsson, and J. Kron, The Influence of Porosity on the Fatigue Strength of High-Pressure Die Cast Aluminium, *Fatigue Fract. Eng. Mater. Struct.*, 2006, **29**(5), p 357–363. https://doi.org/10.1111/j. 1460-2695.2006.00997.x

10. W. Hesse, *Key to Aluminium Alloys*, Aluminium-Verlag, Düsseldorf, 2008, p 88

11. X. Lia, S.M. Xiong, and Z. Guo, Improved Mechanical Properties in Vacuum-Assist High Pressure Die Casting of AZ91D Alloy, *J. Mater. Process. Technol.*, 2016, **231**, p 1–7. https://doi.org/10.1016/j.jmatpro tec.2015.12.005

12. A. Zyska, Z. Konopka, M. Lagiewka, and M. Nadolski, Porosity of Castings Procedure by the Vacuum Assisted Pressure Die Casting Method, *Foundry Eng.*, 2015, **15**(1), p 125–130

13. ISO 6892-1:2016: Metallic materials – Tensile testing – Part1, Method of test at Room Temperature, 2016

14. N.A. Pratten, The Precise Measurement of the Density of Small Samples, *J. Mater. Sci.*, 1981, **16**(7), p 1737–1747

15. ASTM E505-15: Standard Reference Radiographs for Inspection of Aluminum and Magnesium Die Castings, 2015

16. EN 1706:2013-12: Aluminium and Aluminium Alloys – Castings: Chemical Composition and Mechanical Properties, 2013

17. ITS-90 Density of Water Formulation for Volumetric Standards Calibration, *J. Res. Natl. Inst. Stand. Technol.* 1992, **97/3**, p 336–340

18. BN-75/4051-10: Porosity of Casting by Hydrostatic Weighing, 1975

19. C. Maierhofer, P. Myrach, M. Röllig, F. Jonietz, B. Illerhaus, D. Meinel, U. Richter, R. Miksche, Characterization of Pores in High Pressure Die Cast Aluminum Using Active Thermography and Computed Tomography, in *42nd Annual Review of Progress in Quantitative Nondestructive Evaluation*, 2016; p. 1–8, 2016

20. VGStudioMAX 3.2 Software (VG.034-EN.v03_B I 11.2014), Volume Graphics GMBH, Heidelberg, Germany, 2014

21. B. Oberdorfer, E. Kaschnitz, D. Habe, H. Holzer, G. Schindelbacher, P. Schumacher, New Method of Enhanced Quality Assessment for Al-Castings by Computed Tomography, in *Proceedings 5th Conference on Industrial Computed Tomography (iCT) 2014*, Wels, Austria, Shaker Verlag 2014; 133

22. M. Wicke, A. Brueckner-Foit, T. Kristen, M. Zimmermann, F. Buelbuel, and H.-J. Christ, Near-Threshold Crack Extension Mechanism in an Aluminum Alloy Studied by SEM and X-Ray Tomography, *Int. J. Fatigue*, 2019, **119**, p 102–111. https://doi.org/10.1016/j.ijfatig ue.2018.08.024

23. D.C. Jiles, *Introduction to the Principles of Materials Evaluation, Wolfson Center for Magnetic*, Institute for Advanced Materials and Energy Systems, Cardiff University, UK, 2007, p 79–97

24. Y. Tijani, A. Heinrietz, W. Stets, and P. Voight, Detection and Influence of Shrinkage Pores and Nonmetallic Inclusions on Fatigue Life of Cast Aluminum Alloys, *Metall. Mater. Trans. A*, 2013, **44**(12), p 5408–5415. https://doi.org/10.1007/s11661-013-1773-0

25. I. Koutiri, D. Bellett, F. Morel, L. Augustins, and J. Adrien, High Cycle Fatigue Damage Mechanisms in Cast Aluminum Subject to Complex Loads, *Int. J. Fatigue*, 2013, **47**, p 44–57. https://doi.org/10.1016/j.ijfa tigue.2012.07.008

26. D. Roylance, K.C. Cohen, C.H. Jenkins, and S.K. Khana, *Mech. Mater. A Mater. Sci. Perspect.*, 2001, **215**(3), p 141–145. https://doi.org/10. 1243/1464420011544987

27. J. Campbell, *Castings*, Butterworth-Heinemann, Oxford, 2003, p 314–318

28. A. Ben Ahmed, M.I. Houria, R. Fathallah, and H. Sidhom, The Effect of Interacting Defects on the HCF Behavior of Al-Si-Mg Aluminum Alloys, *J. Alloys Compd.*, 2019, **779**, p 618–629. https://doi.org/10. 1016/j.jallcom.2018.11.282

29. K. Bangyikhan, *Effect of Oxide Film, Fe-Rich Phase, Porosity and Their Interactions on Tensile Properties of Cast Al-Si-Mg Alloys* (PhD thesis of the Faculty of Engineering of The University of Birmingham, 2005). p. 45

30. Y. Tijani, A. Heinrietz, T. Bruder, and H. Hanselka, Quantitative Evaluation of Fatigue Life of Cast Aluminum Alloys by Non-destructive Testing and Parameter Model, *Int. J. Fatigue*, 2013, **57**, p 73–78. https://doi.org/10.1016/j.ijfatigue.2013.05.017

31. P. Mu, Y. Nadot, C. Nadot-Martin, A. Chabod, I. Serrano-Munoz, and C. Verdu, Influence of Casting Defects on the Fatigue Behavior of Cast Aluminum AS7G06-T6, *Eng. Fract. Mech.*, 2014, **131**, p 315–328. https://doi.org/10.1016/j.engfracmech.2014.08.007

32. W.D. Callister, Jr., *Fundam. Mater. Sci. Eng.*, 2001, **2001**, p 261–262